Banner appropriate to article type will appear here in typeset article

Effects of oscillating gas phase flow on an evaporating multicomponent droplet

- 3 Sreeparna Majee¹, Abhishek Saha²† and Saptarshi Basu¹‡
- ⁴ Department of Mechanical Engineering, Indian Institute of Science, Bengaluru, Karnataka 560012, India
- 5 ²Department of Mechanical and Aerospace Engineering, University of California San Diego, La Jolla,
- 6 California 92093, USA
- 7 (Received xx; revised xx; accepted xx)
- 8 The dynamics of an evaporating droplet in an unsteady vortical flow is of practical interest
- 9 to many industrial applications and natural processes. To investigate the transport and
- 10 evaporation dynamics of such droplets, we present a numerical study of an isolated droplet
- in an oscillating gas phase flow. The study uses a one-way coupled two-phase flow model to
- 12 assess the effect of the amplitude and the frequency of a sinusoidal external flow field on the
- 13 lifetime of a multi-component droplet containing a non-volatile solute dissolved in a volatile
- solvent. The results show that the evaporation process becomes faster with an increase in the
- amplitude or the frequency of the gas phase oscillation. The liquid phase transport inside
- the droplet also is influenced by the unsteadiness of the external gas phase flow. A scaling
- the droplet also is influenced by the unsteadiness of the external gas phase flow. A scaling analysis based on the response of the droplet under the oscillating drag force is subsequently
- 18 carried out to unify the observed evaporation dynamics in the simulations under various
- conditions. The analysis quantifies the enhancement in the droplet velocity and Reynolds
- the distriction of the districti
- 20 number as a function of the gas phase oscillation parameters and predicts the effects on the
- 21 evaporation rate.

22 Key words:

23 1. Introduction

- 24 Heat and mass transfers in droplets moving in an unsteady flow are ubiquitous in both
- 25 engineering and geophysical systems. For example, fuel droplets are sprayed in an unsteady
- 26 turbulent flow in internal combustion engines, gas turbines, and liquid-fueled rocket engines
- 27 (Mellor 1980; Law 1982; Birouk & Gokalp 2006; Cantwell et al. 2010; Perini & Reitz
- 28 2016). The unsteady dynamics of evaporation of the droplets and transport of the fuel
- 29 vapor critically affect the subsequent combustion processes and, thus, power or thrust
- 30 generation and ensuing emission. Interaction of unsteady flow and evaporating droplets
- 31 are also present in thermal sprays, where the injected droplets carrying functional materials
- 32 undergo evaporation, precipitation, and chemical transformation in either a turbulent plasma
 - † Email address for correspondence: asaha@eng.ucsd.edu ‡ Email address for correspondence: sbasu@iisc.ac.in

59

60

61

62

63

64 65

66

67

69 70

71

72

73

74

75

76

77

78

79

80 81

82

(Solution Precursor Plasma Process) (Pawlowski 2009; Jordan et al. 2015) or a High-Velocity 33 34 Oxy-Fuel flame environments (Li & Christofides 2009; Basu & Cetegen 2008). Irrespective of the method, the quality of the coating generated with thermal sprays depends on the 35 evaporation dynamics and droplet lifetime (Basu et al. 2008; Saha et al. 2009a, 2010). 36 37 Among geophysical systems, the unsteady flow in the upper atmosphere has a strong influence on the formation of raindrops and clouds. Atmospheric turbulence, indeed, is critical in 38 39 accumulating or dispersing particles that serve as nucleation sites for water vapor to condense and form clouds and raindrops (Shaw et al. 1998; Vaillancourt & Yau 2000; Shaw 2003; 40 Ruehl et al. 2008; Grabowski & Wang 2013). Recently droplet evaporation and transport in 41 an unsteady flow have gained great interest due to their direct relation to the transmission of 42 COVID-19, a disease whose virus primarily transmits through respiratory droplets. Studies 43 44 have been performed to account for the unsteady turbulent jet and puff emanating from oral and nasal cavities along with the respiratory droplets (Mittal et al. 2020; Balachandar et al. 45 2020; Bourouiba 2021; World Health Organization 2020; Jayaweera et al. 2020; Chaudhuri 46 et al. 2020a), to understand their effect on evaporation patterns (Chaudhuri et al. 2020a; 47 Basu et al. 2020; Bourouiba 2020; Rosti et al. 2021; Saha et al. 2022) and build disease 48 transmission models (Chaudhuri et al. 2020b). Simultaneously, several studies focused on 49 the unsteady dynamics of ambient airflow and their influence on the transport of respiratory 50 droplets (Chong et al. 2021; Ng et al. 2021; Dbouk & Drikakis 2020; Sharma et al. 2022). 51 For example, Chong et al. (2021) and Ng et al. (2021) have shown that the unsteadiness 52 in local flow patterns and humidity can lead to growth and clustering among the dispersed 53 respiratory droplet. Other studies (Somsen et al. 2020; Bhagat et al. 2020) investigated how 54 spatial and temporal variation in indoor air can influence the transport of these respiratory 55 droplets and hence, the transmission of the disease. 56 57

The above review of the literature demonstrates that droplet evaporation in unsteady conditions is, indeed, of interest to various engineering, health, and atmospheric problems. Naturally, the fundamental aspects of droplet evaporation received attention in the thermalfluids community. Droplet evaporation in a steady or weakly unsteady environment has been extensively studied in a wide range of situations and configurations, using both theories, experiments, and simulations. These studies paved the way for a detailed understanding of the topic, which was periodically summarized in review articles (Law 1982; Sirignano 1983; Aggarwal & Peng 1995; Sazhin 2006, 2017; Saha et al. 2018). Droplet evaporation in an unsteady flow field has also received attention from the research community. The interaction between a vortex and a droplet with comparable length-scales are studied by Kim et al. (1995), where they investigated the variations in the droplet drag coefficient due to the droplet-vortex interplay. Masoudi & Sirignano (2000) investigated the influence of droplet-vortex collision on the simultaneous heating, evaporation, and mass transfer of the droplet. The interaction of evaporating droplets with a Kármán vortex sheet is studied by Burger et al. (2006) to predict a complex vapor-air mixing process. Fundamental studies with particle dispersion and phase interaction in large vortex structures are also addressed by researchers (Aggarwal et al. 1996; Harstad & Bellan 1997; Kim et al. 1997; Lazaro & Lasheras 1992; Marcu & Meiburg 1996; Tang et al. 1992). It was shown that the dynamics of vortex structures typically govern the mass and momentum exchanges of the droplet dynamics (Clemens & Mungal 1995). Moreover, the dispersion of spray droplets is highly dependent on the surrounding vortex dynamics, and local shearing vortices tend to govern the response behavior of the droplets (Reveillon & Vervisch 2005).

While the above studies have illustrated droplet dynamics in a complex unsteady non-uniform vortical flow field, they were mostly performed for droplets containing pure liquid. However, in many applications, the droplet liquid contains non-volatile dissolved components. In this work, we describe a framework to study the evaporation dynamics of

an isolated binary droplet (containing solvent and solute) in a simpler unsteady oscillating flow field. The primary goal is to identify the response in droplet evaporation rate and the underlying mechanistic description for such response. Finally, we will show similarity and dissimilarity among the responses under various unsteady conditions using proper non-dimensional timescales. We will accomplish these goals by formulating a two-dimensional numerical model for binary droplets, assuming one-way coupling between the droplet and the periodic perturbation in gas phase velocity. This model, which was originally developed by Abramzon & Sirignano (1989), provides a complete analysis with a detailed numerical simulation for the liquid phase coupled with the gas phase governing the droplet dynamics moving in the air. We have imposed an unsteady gas phase flow condition to simulate the oscillating flow. The cornerstone of this article is the development of a theoretical relation between gas phase frequency and the droplet velocity responsible for the modified evaporation of the oscillating droplet motion.

2. Mathematical modeling

The motion of any respiratory droplet moving in unsteady flow can be described by the drag force experienced by the droplet due to its relative velocity with the surrounding gas phase. The transport of these droplets depends on the perturbation characteristics of the unsteadiness that interacts periodically with the droplets. Moreover, the evaporation of any binary fluid is an intricate process due to the complex heat and mass transfer in the gas phase and liquid phase, where the latter is affected by the spatial distribution of the non-volatile solute and solvent concentration. The two-dimensional model used in this work uses a detailed description of liquid phase transport, which on many occasions, is ignored due to computational complexities. The mathematical modeling framework is adapted from Abramzon & Sirignano (1989) for the evaporation of a moving droplet extending the classical droplet evaporation model under the influence of Stefan flow (blowing) on heat and mass transfer and the effect of internal circulation in the liquid phase of the droplet. We will, next, describe the model and its governing equations.

First, we will look into the global transport of the droplet by solving the drag equation. The complete descriptions of the drag equations are given below,

$$\frac{dU_p}{dt} = \frac{3C_D}{8r_s} \left(\frac{\rho_g}{\rho_l}\right) \mid U_g - U_p \mid (U_g - U_p)$$
 (2.1)

$$\frac{dX_p}{dt} = U_p \tag{2.2}$$

$$\frac{dV_p}{dt} = \frac{3C_D}{8r_s} \left(\frac{\rho_g}{\rho_l}\right) | V_g - V_p | (V_g - V_p) + \frac{(\rho_l - \rho_g)}{\rho_l} g$$
 (2.3)

$$\frac{dY_p}{dt} = V_p \tag{2.4}$$

where X_p (or Y_p) and U_p (or V_p) are the horizontal (or vertical) displacement and the instantaneous velocity of the droplet, respectively. U_g and V_g are the gas phase velocities in the horizontal and vertical directions, respectively. Generally, the body force is accounted for using g, the gravitational acceleration. ρ_g and ρ_l are densities of the gas phase and liquid phase, respectively. The liquid phase density is calculated based on the mass fractions of the components. Since the overall solute concentration changes with time due to evaporation, ρ_l is not constant with time. r_s is the instantaneous radius of the droplet. μ_g is gas phase dynamic viscosity. Since we are interested in capturing the unsteady perturbation of one

dimension of the gas phase flow, we assumed vertical gas phase flow is weak ($V_g = 0$) and neglected the body force term (g = 0). The drag forces from the added-mass effects and Basset history force (Berlemont *et al.* 1990; Odar & Hamilton 1964) for our simulation conditions are relatively weak, and hence we have neglected their contributions. See supplementary material for the details. The simplified above drag equation can, then, be linearized for Stokes flow conditions by setting the drag coefficient, $C_D = 24/Re_p$, where the gas phase Reynolds number is defined as,

$$Re_{p} = 2\rho_{g} \mid U_{g} - U_{p} \mid r_{s}/\mu_{g}. \tag{2.5}$$

135 Under these conditions, the droplet motion is described by

136
$$\frac{dU_p}{dt} = \frac{9}{2\tau}(U_g - U_p), \quad \tau = \frac{\rho_l r_s^2}{\mu_g}, \tag{2.6}$$

where τ is the droplet response time. Now, to assess the response of the isolated droplet exposed to an oscillating gas flow field, the gas velocity U_g in Eq. (2.6) is assumed to have a sinusoidal perturbation

$$U_g = U_{g,0} + a\sin(\omega t) \tag{2.7}$$

where $U_{g,0}$ is the mean gas phase velocity; a is the amplitude and $\omega (= 2\pi f)$ is the angular frequency, and f is the frequency of oscillation in gas phase velocity.

Next, we describe the heat and mass transfer part of the model. The change in droplet radius due to the evaporation is defined as

$$\frac{dr_s}{dt} = -\frac{\dot{m}}{4\pi\rho_l r_s^2}. (2.8)$$

In the vapor phase during droplet evaporation, the average temperature is defined to be $T_{mean} = (2T_s + T_{\infty})/3$ as suggested by Hubbard *et al.* (1975), where T_s and T_{∞} are respectively the droplet surface temperature and temperature of the gas phase. By assuming the vapor phase surrounding the liquid droplet as a quasi-steady-state condition, the expressions for evaporation mass flux (heat and mass transfer limits) are given as

$$\dot{m} = 2\pi \rho_{\nu} D_{\nu} r_s Sh^* log (1 + B_M)$$
(2.9)

$$\dot{m} = 2\pi \rho_{\nu} \alpha_g r_s N u^* log (1 + B_T) \tag{2.10}$$

where \dot{m} is the rate of change of droplet's liquid mass due to evaporation, ρ_{v} is the density 154 of water vapor, D_v is the binary diffusivity of water vapor in the air, and α_g is the thermal 155 diffusivity of surrounding air. Here, $B_M = (Y_{w,s} - Y_{w,\infty})/(1 - Y_{w,s})$ and $B_T = C_{p,l}(T_{\infty} - Y_{w,\infty})$ 156 T_s)/ $(h_{fg} - \dot{Q}_l/\dot{m})$ are the Spalding mass and heat transfer numbers. Here, $Y_{w,s}$ and $Y_{w,\infty}$ are 157 the water vapor fraction at the droplet surface and far field, respectively. $C_{p,l}$ and $h_{f,g}$ are the 158 specific heat of the droplet and latent heat for evaporation of the droplet. Q_I is the amount of 159 heat transferred to or from the droplet. Further details can be found in (Abramzon & Sirignano 160 1989; Majee et al. 2021). In Eqs. 2.9 and 2.10, Nu^* and Sh^* are the modified Nusselt and 161 Sherwood numbers. Using the quasi-steady assumption, the Nusselt and Sherwood numbers 162 for a non-evaporating sphere can be defined as (Clift et al. 2005) 163

$$Nu_0 = 1 + (1 + Re_p Pr)^{1/3} f(Re)$$
 (2.11)

$$Sh_0 = 1 + (1 + Re_p Sc)^{1/3} f(Re)$$
 (2.12)

where $Pr(=\mu_g/(\alpha_g\rho_g))$ and $Sc(=\mu_g/(D_v\rho_g))$ are Prandlt and Schmidt numbers respec-

tively. f(Re) is the correction factor for the Reynolds number effect. The correction is

$$f(Re_p) = 1, \ Re_p \leqslant 1 \tag{2.13}$$

171
$$f(Re_p) = Re_p^{0.077}, \ 1 < Re_p \le 400 \tag{2.14}$$

Two physical effects distinguish the heat and mass transfer in evaporating droplets from that of steady-state non-evaporating spheres. First, the surface-blowing effect due to evaporation changes the boundary layer. Furthermore, there exists an asymmetry in the boundary layer along the droplet interface at various angular locations that causes an asymmetry in local heat and mass transfer. Abramzon & Sirignano (1989) accounted for these effects by correcting the Nusselt and Sherwood numbers and, thereby, the global heat and mass transfer rates. Nu^* and Sh^* , the corrected Nusselt and Sherwood numbers can be expressed as,

$$Nu^* = 2 + \frac{Nu_0 - 2}{F(B_T)} \tag{2.15}$$

180 and

$$Sh^* = 2 + \frac{Sh_0 - 2}{F(B_M)},\tag{2.16}$$

where, $F(B) = (1 + B)^{0.7} (\ln(1 + B))/B$. Further details are provided in their works by Abramzon & Sirignano (1989), and Sirignano (2010).

In a binary droplet, the non-volatile component suppresses the vapor pressure of the volatile component at the droplet surface. This phenomenon is taken into account by considering an ideal solution that obeys Raoult's Law (Van Wylen & Sonntag 1978), $P_{vap}(T_s, \chi_{w,s}) = \chi_{w,s}P_{sat}(T_s)$, where $\chi_{w,s}$ is the mole fraction of volatile solvent at the droplet surface in the liquid phase. We note that, for non-ideal solutions, the vapor pressure of the evaporating species at the droplet surface can be evaluated by considering the activity coefficients of each species in the mixture as discussed in several studies (Senda *et al.* 2000; Bader *et al.* 2013; Chen *et al.* 2016; Borodulin *et al.* 2019; Fang *et al.* 2019).

After the mass evaporation rate of the droplet, we will now look into the liquid phase to understand the spatio-temporal temperature and concentration distribution of the evaporating droplet. In this work, any possible deformation in droplet shape due to aerodynamic forces has been neglected. It can be justified by assessing the gas phase Weber number, $We = 2\rho_g(|U_p - U_g|)^2r_s/\sigma$, which is significantly smaller than 1 for the conditions of this study. The surface tension (σ) of the saline water was evaluated as a function of temperature and salt concentration following the correlation derived by Nayar *et al.* (2014). The liquid phase of a spherical droplet translating in the gas phase experiences convective vortical motion due to relative velocity and, thus, shear stress at the liquid-gas interface. Abramzon & Sirignano (1989) showed for such droplets, the internal flow structures can be modeled as the two dimensional well-known Hill's spherical vortex (Lamb 1993). The explicit solution for Hill spherical vortex, then, renders the expressions for the radial and angular velocities in the spherical coordinate system (r, θ) in the liquid phase

$$V_r = -U_s \left(1 - \frac{r^2}{r_s^2} \right) \cos \theta, \tag{2.17}$$

 $V_{\theta} = U_s \left(1 - 2 \frac{r^2}{r_s^2} \right) \sin \theta, \tag{2.18}$

where $U_s = (1/32)(U_g - U_p)(\mu_g/\mu_l)Re_pC_F$ is the liquid velocity at the vapor-liquid interface and is calculated by the continuity of the shear stress across the interface; μ_l is liquid phase dynamic viscosity, and C_F is the skin friction coefficient for an evaporating

sphere calculated using the correlation given by Renksizbulut & Yuen (1983).

$$C_F = \frac{12.69Re_p^{-2/3}}{1 + B_M} \tag{2.19}$$

It is to be noted that thermal and concentration gradient across the droplet interface can induce Marangoni stress, which can be important for modeling the evaporation of multicomponent droplets (Niazmand *et al.* 1994; Dwyer *et al.* 1996, 1998). However, for the present study, the gradients are small, and as such, the Marangoni flow velocity is expected to be smaller

than the shear-driven flow (U_s) at the droplet surface. A detailed comparison is shown in the supplementary material.

The non-dimensional conservation equations of energy and mass fraction in the liquid phase are given by (Ozturk & Cetegen 2004)

221
$$\overline{r_s^2} \frac{\partial \overline{T}}{\partial \overline{t}} + (0.5Pe_l \overline{V_r} \overline{r_s} - \beta \eta) \frac{\partial \overline{T}}{\partial \eta} + 0.5Pe_l \overline{V_\theta} \overline{r_s} \frac{\partial \overline{T}}{\partial \theta}$$

$$= \frac{1}{\eta^2} \frac{\partial}{\partial \eta} \left(\eta^2 \frac{\partial \overline{T}}{\partial \eta} \right) + \frac{1}{\eta^2 sin\theta} \frac{\partial}{\partial \theta} \left(sin\theta \frac{\partial \overline{T}}{\partial \theta} \right)$$
(2.20)

223 and

224
$$Le_{l}\overline{r_{s}^{2}}\frac{\partial\overline{Y_{N}}}{\partial\overline{t}} + (0.5Pe_{l}Le_{l}\overline{V_{r}}\overline{r_{s}} - Le_{l}\beta\eta)\frac{\partial\overline{Y_{N}}}{\partial\eta} + 0.5Pe_{l}Le_{l}\frac{\overline{V_{\theta}}\overline{r_{s}}}{\eta}\frac{\partial\overline{Y_{N}}}{\partial\theta}$$

$$= \frac{1}{\eta^{2}}\frac{\partial}{\partial\eta}\left(\eta^{2}\frac{\partial\overline{Y_{N}}}{\partial\eta}\right) + \frac{1}{\eta^{2}sin\theta}\frac{\partial}{\partial\theta}\left(sin\theta\frac{\partial\overline{Y_{N}}}{\partial\theta}\right), \qquad (2.21)$$

respectively. Eq. (2.20) and Eq. (2.21) are solved using the initial and boundary conditions,

$$\overline{t} = 0 \to \overline{T} = 0$$

$$\eta = 1, \begin{cases} \frac{\partial \overline{T}}{\partial \theta} = 0 \\ \int_0^{\pi} \frac{\partial \overline{T}}{\partial \eta} \sin\theta d\theta = \frac{Q_t}{2\pi r_s k_l T_0} \end{cases}$$

$$\theta = 0, \pi \to \frac{\partial \overline{T}}{\partial \theta} = 0,$$
(2.22)

228 and

229
$$\begin{aligned}
\overline{t} &= 0 \to \overline{Y_N} &= 0 \\
\eta &= 1, \begin{cases} \frac{\partial \overline{Y_N}}{\partial \theta} &= 0 \\
\int_0^{\pi} \frac{\partial \overline{Y_N}}{\partial \eta} \sin\theta d\theta &= \frac{\dot{m}}{2\pi \rho_l r_s D_{v,za} Y_{N,0}}, \\
\theta &= 0, \pi \to \frac{\partial \overline{Y_N}}{\partial \theta} &= 0,
\end{aligned} \tag{2.23}$$

respectively. Here, $\overline{r_s} = r_s/r_0$ is the non-dimensional droplet radius; $\eta = r/r_s$ is the non-dimensional radial coordinate; $\overline{V_r} = V_r/U_s$ and $\overline{V_\theta} = V_\theta/U_s$ are the non-dimensional velocities (radial and angular, respectively); $\overline{T} = (T - T_0)/T_0$ is the non-dimensional temperature; $\overline{t} = \alpha_l t/r_0^2$ is the non-dimensional time; $\beta = 0.5 \partial \overline{r_s}/\partial \overline{t}$ is the non-dimensional parameter proportional to the droplet's surface regression rate as it vaporizes; α_l is thermal diffusivity of the liquid phase, and \dot{Q}_l is the heat transferred into the liquid. $\overline{Y_N} = (Y_N - Y_{N,0})/Y_{N,0}$ is the normalized mass fraction of the solute, k_l is the thermal conductivity

of the liquid phase and $D_{v,za}$ is the mass diffusivity of solute in water. $Pe_l(=r_s|U_g-U_p|/\alpha_l)$ and $Le_l(=D_{v,za}/\alpha_l)$ are the Péclet number calculated based on liquid properties and Lewis number of the liquid phase, respectively.

The above set of equations of the model shows that the liquid phase transport affects the temperature and concentration at the droplet surface. This, in turn, affects the evaporation rate and, thus, droplet size. Droplet size, on the other hand, determines the drag forces, which control the velocity and acceleration of the droplet. The instantaneous droplet velocity affects the heat and mass transfer in the gas phase and hence, the evaporation rate. Both gas phase and liquid phase properties play critical roles in determining the relative effects of these complex coupled processes. In summary, the evaporation of an isolated droplet moving in the gas phase, indeed, involves complex coupled processes.

All the above Eqs. (2.1-2.23) are solved numerically, both for external vapor and internal liquid regions. However, in order to solve the liquid phase, boundary conditions presented in Eq.(2.22) and (2.23), need values from the vapor phase solution. Therefore, a numerical integration method using a forward marching scheme is implemented to solve Eq. (2.1). Moreover, the instantaneous droplet radius (Eq. (2.8)) is also computed by a forward marching scheme using the mass flux \dot{m} generated from Eq. (2.9). Furthermore, \dot{Q}_l is solved using Spalding heat transfer number B_T and both \dot{Q}_l and \dot{m} is employed in the boundary conditions (Eq. 2.22 and 2.23).

After deriving the boundary conditions from the vapor phase solution, the energy (Eq. 2.20) and species (Eq. 2.21) conservation equations of the droplet's liquid phase along with the boundary conditions (Eq. 2.22 and 2.23) are numerically computed by a fully implicit iterative finite difference scheme called standard second-order Peaceman–Rachford ADI method (Peaceman & Rachford 1955). The details of the numerical algorithm used in this work can be found in Majee *et al.* (2021). The consideration of an implicit scheme guarantees an unconditionally stable method. It is to be noted that the liquid phase inside the droplet was solved using a polar $(r - \theta)$ coordinate system, where both the dimensions were discretized using an equal number (20 for this study) of grid points, leading to $\Delta \eta = 0.05$, and $\Delta \theta = 0.157$ were taken for the entire simulation process. We have performed a grid convergence study using various grid sizes (see the supplementary materials for details). We used a time step of $\Delta t = 0.0001$, which is short enough to capture the transport processes. The property values used for this study can be found in the supplementary materials.

3. Results and discussion

As mentioned before, the primary goal of this work is to assess the response in droplet evaporation rate under various degrees of oscillations in gas phase velocity, given by Eq. 2.7. This will be attained by modulating the frequency (f) and amplitude (a) of the oscillation. As for the binary droplet, we assumed it contains 1%(w/w) of NaCl (solute) dissolved in water (solvent). Here, we note that a wide range of solute-solvent combinations can be selected for such a study. However, we chose the NaCl solution because (1) it is easily available for experimental validation and (2) it closely resembles surrogate respiratory fluids (Vejerano & Marr 2018; Basu et al. 2020). Similarly, a wide range of ambient (temperature and humidity) conditions could be selected for this study. However, we used conditions that closely resemble that of our ambient air $(T_{amb} = 301K \text{ and } RH_{amb} = 48\%)$.

3.1. Model validation

To validate the model, we will first compare the numerical result with a simple experimental setup. The experiments were conducted by measuring the evaporation rate of an isolated acoustically levitated droplet with 1% w/w NaCl-aqueous solution in $301 \pm 0.2K$ ambient

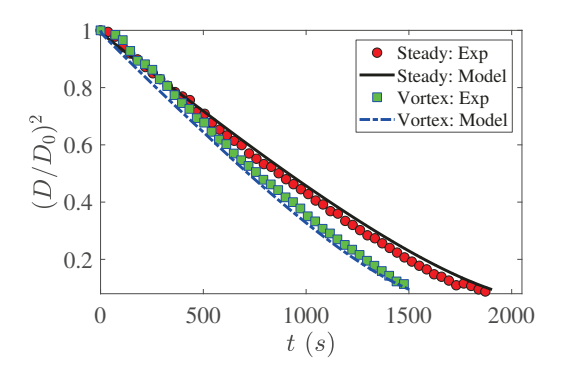


Figure 1: Model validation: comparison of diameter regression, $(D/D_0)^2$, between experimental (levitated droplet) and model data. 'Steady' represents experiments with no vortical flow. 'Vortex' represents experiments with vortical flow over a levitated droplet. In experiments, the initial droplet diameter is $D_0 = 1.8mm$.

temperature and $48 \pm 1\%$ relative humidity. For these experiments, the droplets were at the same temperature as the surrounding air (301K). Air vortex rings were generated with amplitude a = 1.9m/s and frequency f = 5Hz and are made to interact with the levitated droplet of initial diameter $D_0 = 1.8mm$. The mean flow in the experimental setup is 0.3m/s. The details of these experiments are provided in Sharma *et al.* (2021, 2022). Experimentally, we can only measure the droplet diameter as a function of time, which has been compared with the model for two cases, with the vortex (unsteady case) and without the vortex (steady case). Since the precipitation kinetics was not included in the current approach, the comparison was performed until the maximum local concentration of the solution (NaCl in this case) reached the critical value $Y_{N,S}$ (=0.393 for NaCl). Nevertheless, Fig. 1, which shows the $(D/D_0)^2$ vs. t comparisons between the experiments and the model, confirms that they show reasonably good agreement. Similar agreements were also observed for other amplitude and frequency cases. Thus, we are confident that the model can capture the effects of unsteady gas flow on the evaporation dynamics of an isolated droplet.

3.2. Evaporation dynamics of the droplet

In the rest of the manuscript, we will discuss the results from the model to illustrate the effect of a broad range of periodic oscillations in the gas phase velocity on the evaporation dynamics of an isolated droplet. As mentioned before, we will keep the ambient condition fixed with $(RH)_{amb} = 48\%$ and $T_{amb} = 301K$. The initial droplet temperature was taken as 303K, which closely resembles the temperature of respiratory droplets ejected during respiratory events (Carpagnano *et al.* 2017). To avoid a negative gas phase velocity, the mean velocity of the gas phase was kept equal to the amplitude of the gas phase oscillation, i.e. $U_{g,0} = a$.

We will now present the diameter regression rate for various degrees of flow oscillation for two different droplet sizes. First, we compare the evaporation dynamics of a $100\mu m$ droplet under various frequencies of oscillation at amplitude (a) of 0.1 m/s (Fig. 2a) and 1 m/s (Fig. 2b). We observed that for a lower amplitude of perturbation (a = 0.1 m/s), the deviation in D/D_0 with the steady (a = 0) case is minimal compared to the high amplitude (a = 1 m/s) case. Although with an increase in frequency, the evaporation time becomes shorter for the low amplitude oscillations, the difference between various frequencies is minimal (Fig. 2a). For larger amplitude, however, we see almost 30% decrease in time for $(D/D_0)^2$ to reach 0.1 (approximately when precipitation is triggered) for f = 30Hz compared to f = 1Hz, as shown in Fig. 2b. Next, we compare the same amplitude and frequency of oscillations for a

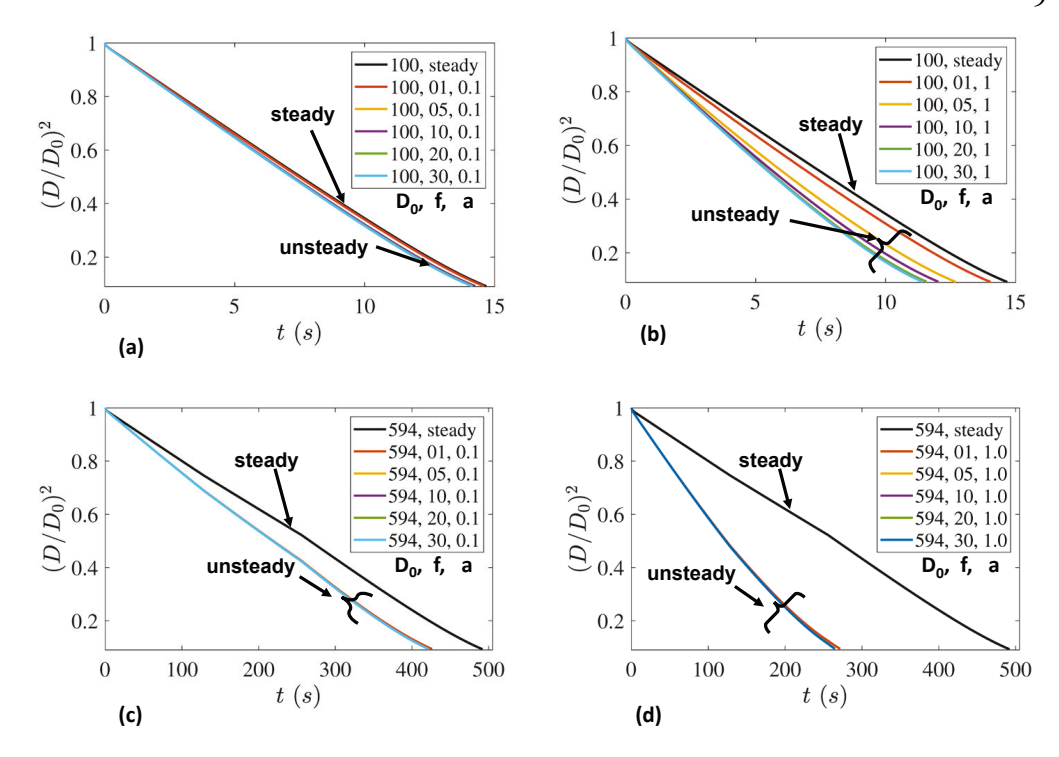


Figure 2: Normalized droplet diameter as a function of time for various combinations of initial droplet diameters (D_0) , amplitude (a), and frequency (f) of gas phase oscillation. (a) $D_0 = 100 \mu m$ and a = 0.1 m/s, (b) $D_0 = 100 \mu m$ and a = 1 m/s, (c) $D_0 = 594 \mu m$ and a = 0.1 m/s, and (d) $D_0 = 594 \mu m$ and a = 1 m/s. Legends: 'steady': no gas phase oscillation; D_0 initial droplet diameter in μm ; f: frequency in Hz; a: amplitude in a:

larger droplet ($D_0 = 594\mu m$) in Figs. 2c and d. We observe similar behavior in that an increase in amplitude and frequency increases the evaporation rate. However, for both amplitudes, we don't observe significant changes in evaporation rate across various frequencies from 1-30Hz. Nevertheless, the evaporation is much faster with oscillations (non zero a) than the *steady* (a=0) case (14% for a=0.1m/s and 40% for a=1m/s). The cause of such varying influence of oscillation on the evaporation rate for different droplet sizes and oscillation parameters will be discussed later in the context of the modified Reynolds number.

3.3. Velocity of gas phase and droplet motion

The comparisons in the previous subsection show that the effect of oscillation in gas phase velocity on the evaporation rate is non-linear. We note that the evaporation rate of the droplet strongly depends on the Nusselt and Sherwood numbers (Eq. 2.9-2.10), which depend on the droplet Reynolds numbers (Eq. 2.11-2.16), and hence the relative velocity between the droplet and the surrounding gas phase (Eq. 2.5). Thus, we investigate the effects of oscillation in gas phase velocity on the bulk velocity of the droplet. In Fig. 3 and 4, we compare the instantaneous gas phase velocity (U_g) and droplet velocity (U_p) during the evaporation process for two different droplet diameters and frequencies of oscillation. In both cases, the mean velocity ($U_{g,0}$) and amplitude (a) of the gas phase flow were maintained to be 1m/s. For smaller droplets ($D_0 = 100\mu m$) and lower frequency oscillation (f = 5Hz), we observe the droplet velocity (U_p) to exhibit a periodic behavior as well (Fig. 3). The left inset of Fig. 3, which shows the zoomed view of the initial 1s of the droplet lifetime,

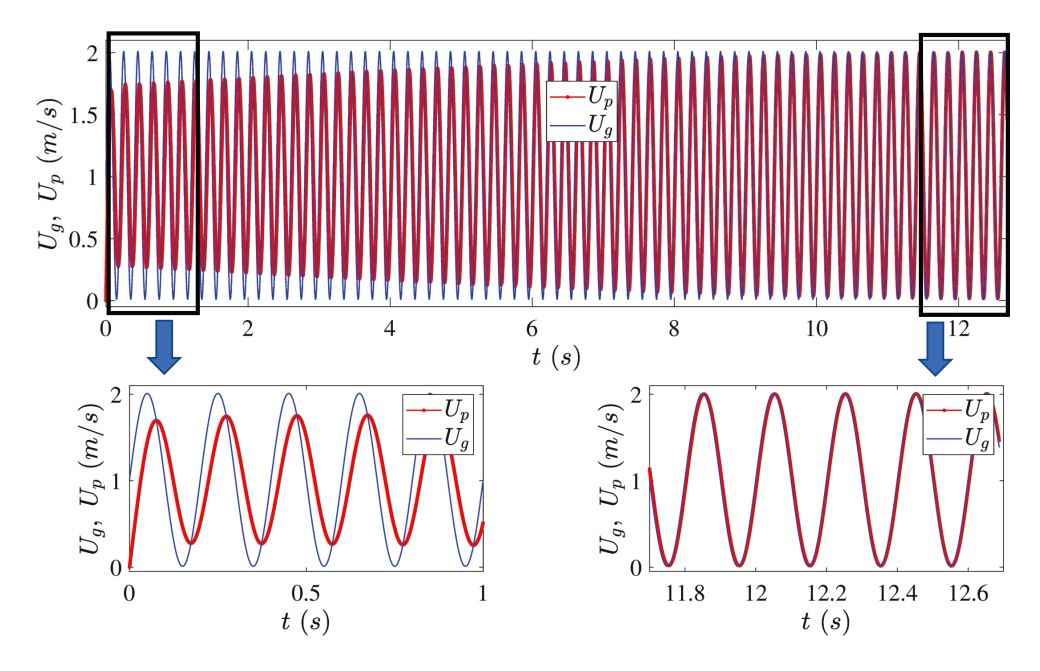


Figure 3: The instantaneous velocities of the gas phase (U_g) and the droplet (U_p) as function of time for initial droplet size $D_0 = 100\mu m$. The gas phase oscillation has amplitude a = 1m/s and frequency of f = 5Hz.

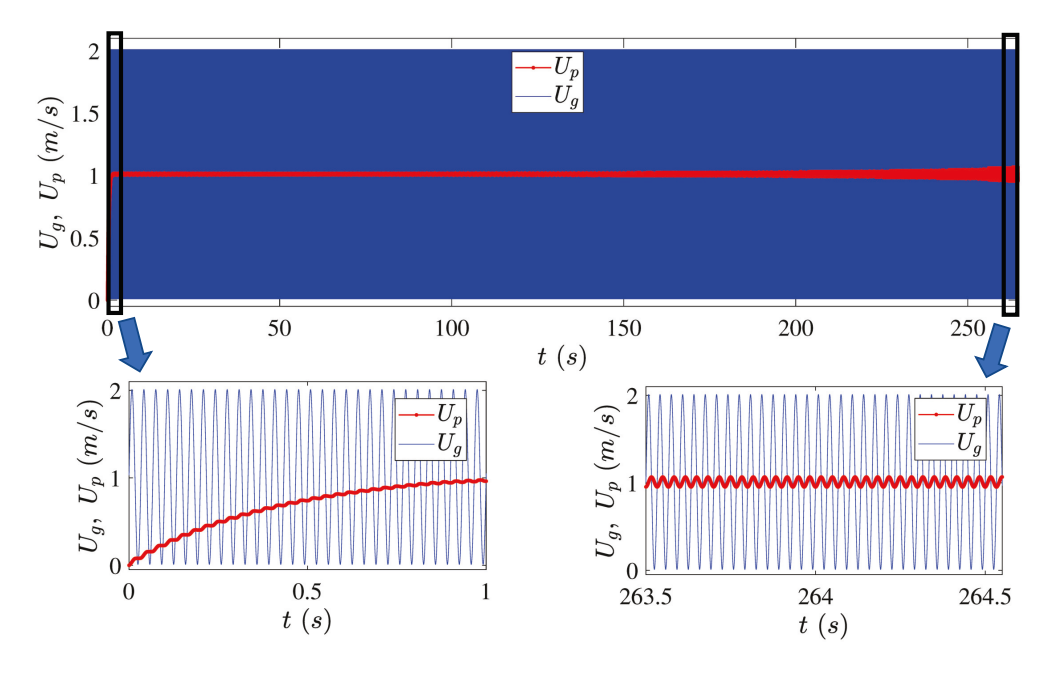


Figure 4: The instantaneous velocities of the gas phase (U_g) and the droplet (U_p) as function of time for initial droplet size $D_0 = 594 \mu m$. The gas phase oscillation has amplitude a = 1m/s and frequency of f = 30Hz.

confirms that initially, the amplitude of the induced oscillation in the U_p has an amplitude 337 slightly smaller than that of the gas phase, and the there exists a phase lag. However, at a 338 later stage (right inset in Fig. 3), the difference between the two velocities, gas phase (U_g) 339 and droplet (U_p) , becomes negligible, and their oscillations become almost identical both 340 in phase and amplitude. On the other hand, for a larger droplet ($D_0 = 594 \mu m$) and higher 341 342 frequency (f = 30Hz) of oscillation, we observe different dynamics (Fig. 4). In particular, 343 the oscillation in droplet velocity takes longer to attain that of the gas phase. Furthermore, we observe much slower growth in the amplitude of oscillation in U_p , which never grows 344 beyond 10% before precipitation is triggered (~265 sec). We also observe a consistent phase 345 lag between the oscillation in U_g and U_p . 346

3.4. Theoretical scaling analysis

347

360

364

365

366 367

In this section, we present a time-scale analysis to understand the observed dynamics of 348 induced oscillation in the droplet velocity (U_p) . For gas phase oscillation of $U_g = U_{g,0} +$ 349 $aSin(2\pi ft)$, we can evaluate the induced oscillation in droplet velocity by integrating the 350 equation for drag (Eq. 2.6) with the initial condition of $U_p = 0$ at t = 0 (initial droplet 351 352 velocity is 0). We recall the definition of the drag coefficient ($C_D = 24/Re_p$), and Reynolds number $(Re_p = 2\rho_g \mid U_g - U_p \mid r_s/\mu_g)$. We can also define $\tau = (\rho_l r_s^2)/\mu_g$, as the response time for a spherical droplet in a viscous flow, and $t_g = 1/f$, as the characteristics time 353 354 scale for gas phase oscillation. The droplet response in an unsteady flow is characterized by 355 Stokes number $St = \tau/t_g$ (Crowe et al. 1998), which represents the ratio of the characteristic 356 timescale for droplet response (τ) to that of the external flow (t_g) . In the context of our 357 study with oscillatory gas phase velocity, the Stokes number can be written as $St = \tau f$. Now 358 substituting these definitions in Eq. 2.6, we get a non-dimensional drag equation, 359

$$\frac{d\left((U_p - U_{g,0})/a\right)}{d(t/t_g)} = -\frac{9}{2St} \left(\frac{U_p - U_{g,0}}{a}\right) + \frac{9}{2St} sin(2\pi \frac{t}{t_g}). \tag{3.1}$$

In the equation above, we notice that the non-dimensional droplet velocity, $(U_p - U_{g,0})/a$, depends on St, which includes the effect of instantaneous droplet radius and t/t_g , a non-dimensional time.

For simplicity, we restrict the analysis to a non-evaporating spherical droplet, and hence, droplet radius (r_s) and the Stokes number (St) are assumed to be constant. Later, we will discuss the effect of this assumption on the obtained results. With this assumption, we can integrate the Eq. 3.1 to find an explicit form of non-dimensional droplet velocity

$$368 \qquad \frac{U_p - U_{g,0}}{a} = \frac{\sin\left(2\pi(t/t_g) - \phi\right)}{\sqrt{1 + (16\pi^2 S t^2/81)}} + \left(-\frac{U_{g,0}}{a} + \frac{4\pi S t/9}{\left(1 + (16\pi^2 S t^2/81)\right)}\right) e^{-\left(9t/(2t_g S t)\right)}$$
(3.2)

where, $\phi = tan^{-1} (4\pi St/9)$. Equation 3.2 depicts the response in velocity of a non-369 evaporating spherical droplet when the surrounding gas phase gas has an oscillatory 370 perturbation. The first term on the right-hand side (RHS) represents the induced oscillation in 371 droplet velocity. We notice that the frequency of the induced oscillation in droplet velocity is 372 the same as the gas phase perturbation $(f \text{ or } 1/t_g)$, while the non-dimensionalized amplitude 373 of the induced oscillation is $A_{osc} = 1/\sqrt{1 + (16\pi^2 St^2/81)}$. The induced oscillation in the 374 droplet velocity lags the oscillation in gas phase velocity by a phase angle, ϕ . The second 375 term in RHS shows the effect of viscous drag, which exponentially reduces the difference 376 377 between the mean velocities of the droplet and the gas phase. It is worth noting that for a steady gas phase flow (i.e. a = 0), the oscillatory term vanishes, and Eq. 3.2 reduces to the 378

403

404

405

406

407

408

409

410 411

412

413

414

415

416

417

419

420

421 422

423

424

425 426

427

classical exponential relation for a non-evaporating droplet (or spherical object) in a gaseous flow field, $U_{p,0} = U_{g,0} \left(1 - e^{-(9t/(2t_gSt))} \right)$. 380

To graphically illustrate the droplet response expressed in Eq. 3.2, we present the contour 381 plot of the normalized droplet velocity, $(U_p - U_{p,0})/a$ for a large range of St (Y-axis) and 382 non-dimensional time, t/t_g (X-axis) in Fig. 5a. Since $U_{p,0}$ is the droplet velocity in a steady 383 gas phase flow, $(U_p - U_{p,0})/a$ measures the modification in droplet velocity due to the 384 unsteady oscillations in the gas phase. Furthermore, we also plotted the amplitude (A_{osc}) 385 and phase (ϕ) of the induced oscillation in droplet velocity as a function of St in Fig. 5b. 386 From the contour plot (5a), we can see that for a small St (<<1), the droplet velocity, 387 $(U_p - U_{p,0})/a$ exhibits a periodic behavior with time, expressed by the color bands in the 388 horizontal direction. The periodicity in the color band appears to be non-uniform due to 389 the log scale used in X-axis. A dominant periodic behavior at small St is expected as the 390 second term in RHS of the Eq. 3.2 is small. The amplitude of the induced oscillation for 391 392 this case ($St \ll 1$) is also high and close to that of the gas phase perturbation ($A_{OSC} \approx 1$) as seen in Fig. 5b. As the St increases and approaches 1, the periodic pattern still exists, but 393 394 the difference between the maximum and minimum instantaneous velocity (color variation in Fig. 5a) becomes weaker due to the reduced amplitude of the induced oscillation (A_{osc} 395 in Fig. 5b). We also notice that the maximum velocity zones (bright yellow zones) in the 396 contour plot shift toward the right. This is the outcome of increased phase lag, ϕ between 397 droplet and gas phase velocities, with St (Fig. 5b). For very large St (>> 1), the denominator 398 399 of the first term in the RHS of Eq. 3.2 becomes significantly greater than unity. As such, the amplitude of the oscillation becomes minimal (A_{OSC} in Fig. 5b). This is why the color 400 variation in the horizontal direction (as a function of time) diminishes at the top half of the 401 contour plot (St >> 1 in Fig. 5a). 402

The above analyses can also be performed by considering the variation in droplet radius due to evaporation. However, such an approach, shown in Appendix A, does not lead to a closed-form expression for droplet velocity. Furthermore, it can be shown (see Appendix) that the difference in the change in droplet velocity due to oscillation $((U_p - U_{p,0})/a)$ evaluated using two approaches (with and without the assumption of constant droplet radius) is relatively insignificant. Hence, we used the constant droplet assumption for the rest of the study.

Now to illustrate the range of St experienced by the evaporating droplets, we plotted the instantaneous St obtained from the simulation of various cases on the theoretical contour plot in Fig. 5a. Since the droplet diameter and hence, τ decreases due to evaporation, the St shows a downward decreasing trend with non-dimensional time (t/t_g) . We observe that the case with a small initial diameter ($D_0 = 100 \mu m$) and the lower frequency oscillation (f = 1, 5Hz) experiences low St and hence, large amplitude oscillations in its velocity (Fig. 5a). This effect is also observed in Fig. 3, where we showed that for $D_0 = 100 \mu m$ and f = 5Hz, the amplitude of oscillation in droplet velocity quickly attains that of the gas phase velocity. As the frequency of oscillation in gas phase velocity (f) increases, the St increases reducing the amplitude of induced oscillation in droplet velocity (f = 1, 5 and 30 Hz in Fig. 5a). For larger droplets ($D_0 = 594 \mu m$), the St becomes significantly greater than unity, and hence, they don't exhibit significant induced oscillations in the velocity. For $D_0 = 594 \mu m$ and f = 30Hz, we observe a weak response, and hence, the amplitude becomes inconsequential to the frequency change (Fig. 4).

Next, we will assess the effect of oscillation in gas phase flow on the Re_p , which, in turn, affects the evaporation rate. Since the external conditions are kept constant in our simulations, the changes in diameter reduction rate observed in Fig. 2a-d is through Sherwood (Sh^*) and Nusselt (Nu^*) numbers in Eqs. 2.9 and 2.10, respectively. Equations 2.11 to

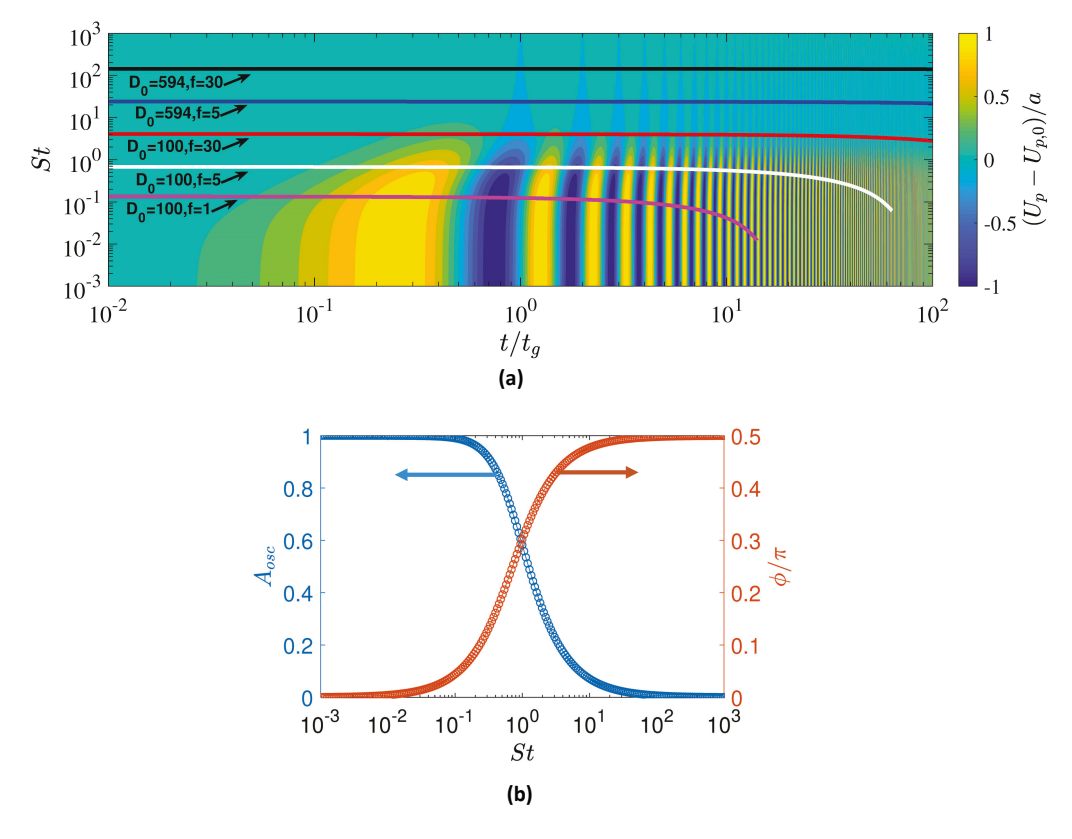


Figure 5: (a) Contour plot of non-dimensional droplet velocity $(U_p - U_{p,0})/a$ with Stokes number (St) and non-dimensional time (t/t_g) , where t_g is the gas phase perturbation time. History of Stokes number (St) for different initial diameters and frequencies are plotted on the contour map. Legends: D_0 is the initial diameter in μm , and f is the frequency of gas phase oscillation in m/s. For all five cases, the amplitude of the gas phase oscillation is a = 1m/s. (b) Variation in amplitude $(A_{OSC} = 1/\sqrt{1 + (16\pi^2 St^2/81)})$ and phase lag $(\phi = tan^{-1} (4\pi St/9))$ of the induced oscillation in non-dimensional droplet velocity $(\frac{U_p - U_{g,0}}{a})$ as function of Stokes number (St).

2.16, subsequently, show that an increase in Re_p , increases both Sh^* and Nu^* , and hence, evaporation rate. Since the Reynolds number (Re_p) is defined based on the relative velocity between the gas phase and the droplet, one can evaluate the induced Re_p due to gas phase velocity oscillation by substituting U_p (Eq. 3.2) and U_g (Eq. 2.7) in Eq. 2.5. Similarly, it is also possible to evaluate the Reynolds number of the droplet without the gas phase oscillation (a=0) as $Re_{p,0}=2\rho_g \mid U_{g,0}-U_{p,0}\mid r_s/\mu_g$. Clearly, higher (or lower) values of the ratio $Re_p/Re_{p,0}$ signify stronger (or weaker) effects of gas phase oscillation on the evaporation rate compared to the steady condition (a=0). Figure 6a shows the contours of this ratio for a range of St and normalized time, t/t_g . Based on the color, the map can be divided (almost diagonally) into two parts separated by the dotted line, St_{crit} . The top-left half, where the instantaneous values of $Re_p/Re_{p,0}$ are close to unity (10° in the plot), represents a zone where the relative effects of gas phase oscillation on Re with respect to $Re_{p,0}$ is small, and hence, can be characterized as "zone of silence." The change in droplet velocity $(U_p - U_{p,0} \approx 0)$ due to gas phase oscillation is, indeed, weak as observed in Fig. 5a. Furthermore, under steady flow conditions, the relative velocity between the droplet and the gas phase (hence,

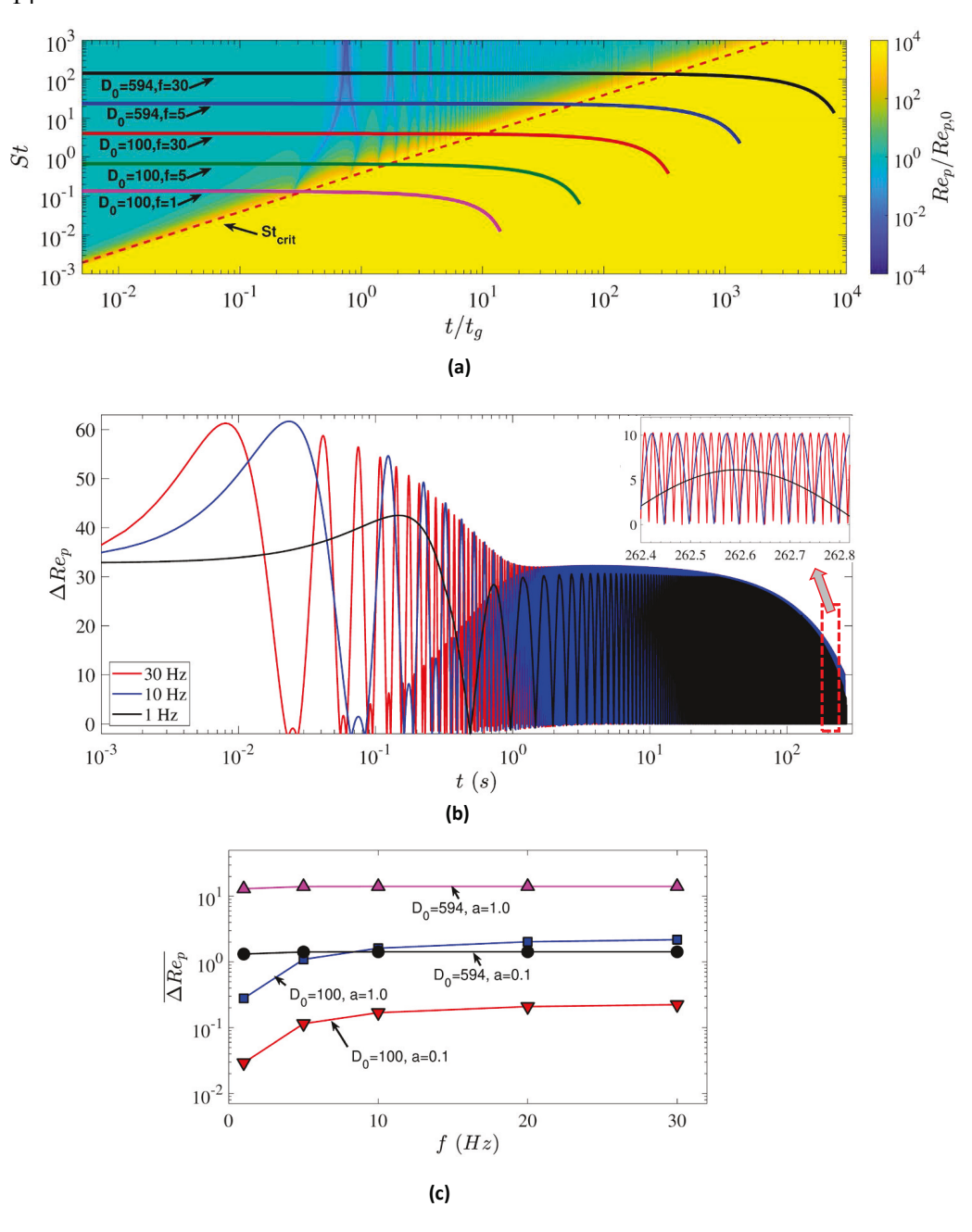


Figure 6: (a) Contour plot for $Re_p/Re_{p,0}$ with Stokes number (St) and non-dimensional time (t/t_g) , where t_g is the gas phase perturbation time. History of Stokes number (St) for different initial diameters and frequencies are plotted on the contour map. Legends: D_0 is the initial diameter in μm , and f is the frequency of gas phase oscillation in m/s. For all five cases, the amplitude of the gas phase oscillation is a = 1m/s. (b) Time history of changes in droplet Reynolds number due to gas phase oscillation $(\Delta Re_p = Re_p - Re_{p,0})$ for amplitude a = 1m/s, frequencies (f = 1, 10, 30Hz). The initial droplet diameter (D_0) is $594\mu m$. (c) The average changes in droplet Reynolds number due to gas phase oscillation $(\overline{\Delta Re_p})$, averaged ΔRe_p) as a function of frequency (f of gas phase oscillation for different amplitudes (a in m/s) and initial droplet diameters (D_0) in μm).

 $Re_{p,0}$) is high. On the other hand, the bottom-right half of Fig. 6a, represents a zone where $Re_p/Re_{p,0}$ has a very high value and hence, can be characterized as a "zone of influence." In this regime, droplet velocity (U_p) displays strong oscillatory behavior as shown in Fig. 5a. Furthermore, under steady gas phase flow (a=0), the differences between the droplet velocity become small and hence, $(Re_{p,0} \rightarrow 0)$. Consequently, for a given t/t_g , the transition between the "zone of silence" and the "zone of influence" can be marked by a critical Stokes number (St_{crit}) for which $U_{p,0} \rightarrow U_{g,0}$. In Fig. 6a, a representative transitional boundary is drawn by setting $(U_{p,0} - U_{g,0})/U_{g,0} = 10^{-5}$. When superimposed the St history from a few selected conditions we simulated, we observe that initially, the droplet starts from the "zone of silence", but transitions into the "zone of influence" (Fig. 6) as time progresses and the droplet becomes smaller due to evaporation.

While $Re_p/Re_{p,0}$ depicts a relative change in Re_p due to oscillation in the gas phase, it is to be recognized that $Re_{p,0} \approx 0$ in the "zone of influence," and as such, the ratio becomes large, even for a small Re_p . To circumvent this bias and to assess the true effect on the evaporation rate, one should evaluate their differences, i.e. $\Delta Re_p = Re_p - Re_{p,0}$. In Fig. 6b, we plotted ΔRe_p as a function of time for a given initial droplet size $(D_0 = 594 \mu m)$ and amplitude (a = 1m/s), but for three different frequencies (f = 1, 10 and 30 Hz) of gas phase oscillation. The plot displays large amplitude oscillations in ΔRe_p at the initial stage. However, the amplitude decays with time and becomes almost constant in the later stage of the droplet lifetime (see inset of Fig. 6b). This behavior, indeed, corroborates with the dynamics of droplet velocity, U_p , described before. To estimate an overall change in Re_p due to oscillation in gas phase flow, we evaluated the mean of ΔRe_p (denoted by $\overline{\Delta Re_p}$) for four combinations of amplitude (a) and initial droplet diameter (D_0) and plotted them as a function of frequency (f) of gas phase oscillation in Fig. 6c. For smaller droplets $(D_0 = 100 \mu m)$ and lower amplitude (a = 0.1 m/s) of oscillation, the $\overline{\Delta Re_p}$ is small $(\sim 10^{-1})$, which explains why we did not observe significant changes in evaporation rate among various frequencies as shown in Fig. 2a. On the other hand, for larger amplitude (a = 1m/s), ΔRe_p is relatively higher (~ 1), and increases with f. Thus, we observed a faster evaporation rate with oscillations, which increases with frequency (Fig. 2b). Figure 6c also confirms that $\overline{\Delta Re_p}$ for larger droplets ($D_0 = 594\mu m$) is higher and remains almost constant for all f, irrespective of the amplitude (a = 0.1 and 1 m/s). This explains the observed faster evaporation under unsteady gas phase flow but the insignificant difference between various frequencies (Fig. 2c and d) for the larger droplets.

3.5. Temperature and concentration distribution in liquid phase

Since our model includes transport equations for the liquid phase, we can compare the temperature and concentration distribution inside the droplet to illustrate the effect of unsteadiness in gas phase velocities on the liquid phase transport. Figures 7 (temperature) and 8 (mass fraction of solute) display the evolution of the internal dynamics for three instances on the lifetime of a $D_0 = 100 \mu m$ droplet and compare it for three different degrees of oscillations in the gas phase. Similar contour plots for $D_0 = 594 \mu m$ are shown in Figs. 9 (temperature) and 10 (mass fraction of solute). Here, we recall that the ambient condition for the simulation was $T_{amb} = 301 K$ and $RH_{amb} = 48\%$, while the initial droplet temperature was set at 303 K and initial solute (NaCl) concentration dissolved in water was $Y_{N,0} = 1\%$. Figures 7 and 9 depict that at the early stage of evaporation, the temperature distribution displays a symmetric concentric profile. This is the hallmark of stronger diffusional transport than advective transport of thermal energy (Abramzon & Sirignano 1989; Sirignano 1983; Saha et al. 2009b) caused by large thermal diffusivity in the liquid phase. The enhanced

thermal transport and smaller initial temperature difference between the gas phase and liquid

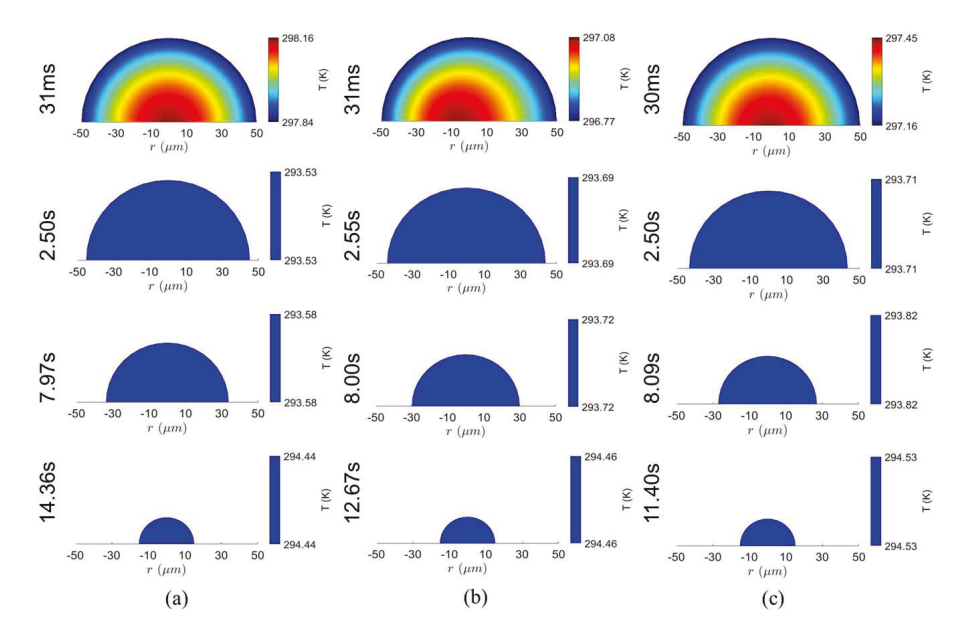


Figure 7: Temperature distribution in liquid phase at different time steps for $D_0 = 100 \mu m$ with initial droplet temperature, $T_0 = 303 K$. The ambient condition is $T_{amb} = 301 K$ and $RH_{amb} = 48\%$. The gas phase perturbation (a) amplitude, a = 0.1 m/s, and frequency, f = 5Hz. (b) a = 1m/s and f = 5Hz. (c) a = 1m/s and f = 30Hz.

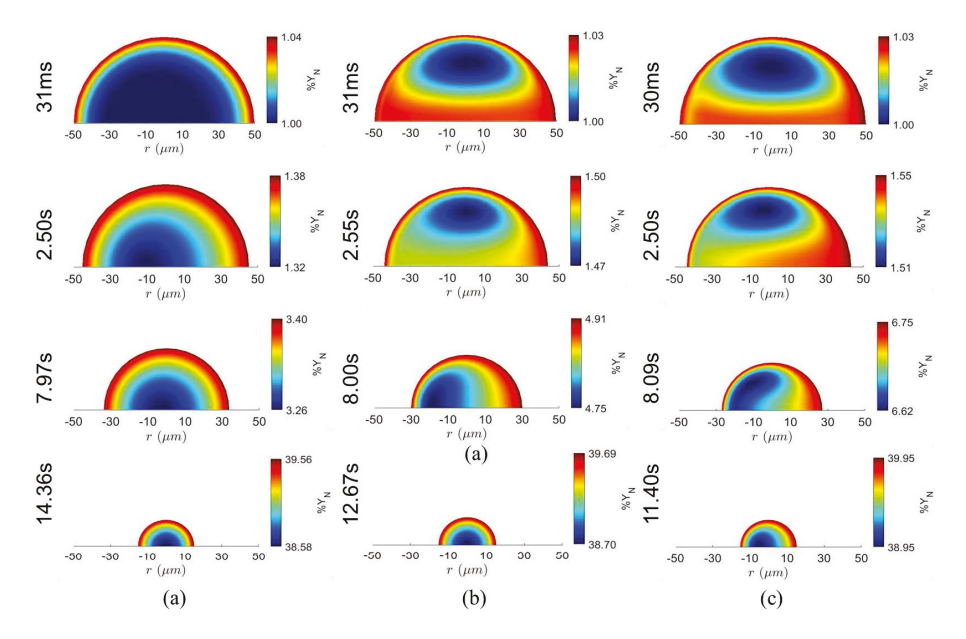


Figure 8: Solute concentration distribution in liquid phase at different time steps for $D_0 = 100 \mu m$ with initial droplet temperature, $T_0 = 303K$. The ambient condition is $T_{amb} = 301K$ and $RH_{amb} = 48\%$. The gas phase perturbation (a) amplitude, a = 0.1 m/s, and frequency, f = 5Hz. (b) a = 1m/s and f = 5Hz. (c) a = 1m/s and f = 30Hz.

phase enable the droplet to reach the wet-bulb temperature and attain homogeneity in a short duration, as seen in both Fig. 7 and 9. Due to the dominant diffusive transport in the liquid phase, the effects of amplitude and frequency of the gas phase oscillation on the temperature profiles are not significant.

Figures 8 and 10 show the concentration distribution of solute in the liquid phase for two different droplet sizes. We notice that the lower amplitude of gas phase oscillation (a = 0.1m/s) leads to a diffusion-dominated concentric distribution even at the early stage of droplet lifetime (Fig. 8a and 10a). On the other hand, for high amplitude oscillations (a =1m/s), a recirculation pattern was formed inside the droplet, which resembles the internal flow pattern (Hill's spherical vortex) (Figs. 8b-c, and Figs. 10b-c). This indicates strong advective transport. The relative strength between advective and diffusive mass transport can be expressed by the Péclet number, $Pe_I = Re_I Sc$, where Sc is the Schmidt number (roughly constant). The liquid phase Reynolds number, Re_l is defined based on the (liquid phase) velocity at the vapor-liquid interface (U_s) driven by gas phase flow or Re_p (Eq. 2.17 and 2.18). As shown in Fig. 5, an increase in the amplitude of oscillation increases Re_p , and hence, Pe_{I} . This is why we observe stronger advective transport for the higher amplitude of gas phase oscillation (Figs. 8 and 10) in the early stage of evaporation. As the droplet evaporates, the Re_p decreases. As such, both Pe_l and the advective transport in the liquid phase become weaker, resulting in more concentric iso-concentration lines for $D_0 = 100 \mu m$ droplets (Figs. 8 b and c.). However, for $D_0 = 594 \mu m$, the Re_l and Pe_l remain comparatively higher throughout the droplet lifetime due to larger droplet diameters. Thus, the convective transport remains strong, as reflected in vortical iso-contours in Figs. 10b and c.

It is to be noted that, for the conditions used in this study, the droplet exhibits almost uniform temperature and concentration distributions except for the initial period of evaporation. One can also employ the rapid mixing model for the liquid phase (Law 1976), which assumes an infinitely fast diffusion process that leads to homogeneous temperature and concentration inside the droplet. Since our goal is to provide a framework that can be used for a wide range of ambient conditions, we used the detailed liquid phase transport model proposed by Abramzon & Sirignano (1989).

4. Summary and outlook

In summary, we have presented a numerical investigation in assessing the effect of oscillation in gas phase velocity on the evaporation rate of an isolated binary droplet. Using a detailed one-way coupled two-phase model, we demonstrated that the evaporation rate increases with the amplitude and frequency of gas phase oscillations and that the influence of oscillation becomes stronger for larger droplets. Subsequently, a scaling analysis illustrated that the oscillation in gas phase velocity induces an oscillatory response in the instantaneous droplet velocity, whose amplitude, frequency, and phase lag depends on three-time scales, leading to two nondimensional parameters, Stokes number (ratio of inertial vs. time period of oscillation) and normalized time (ratio of physical time and the time period of oscillations).

Subsequently, a theoretical estimate of augmentation in the droplet Reynolds number was performed based on the scaling of the induced droplet velocity. Furthermore, the effects of the amplitude and the frequency of oscillation in gas phase velocity on the increase in effective Reynolds number were evaluated. An increase in Reynolds number was shown to induce faster gas phase transport at the droplet interface, which explains enhanced evaporation rate for higher amplitude and frequency of gas phase oscillations. Finally, we discussed transport processes inside the droplet to show that gas phase oscillation has minimal effect on liquid phase thermal transport due to high thermal diffusivity and hence, diffusive transport. The

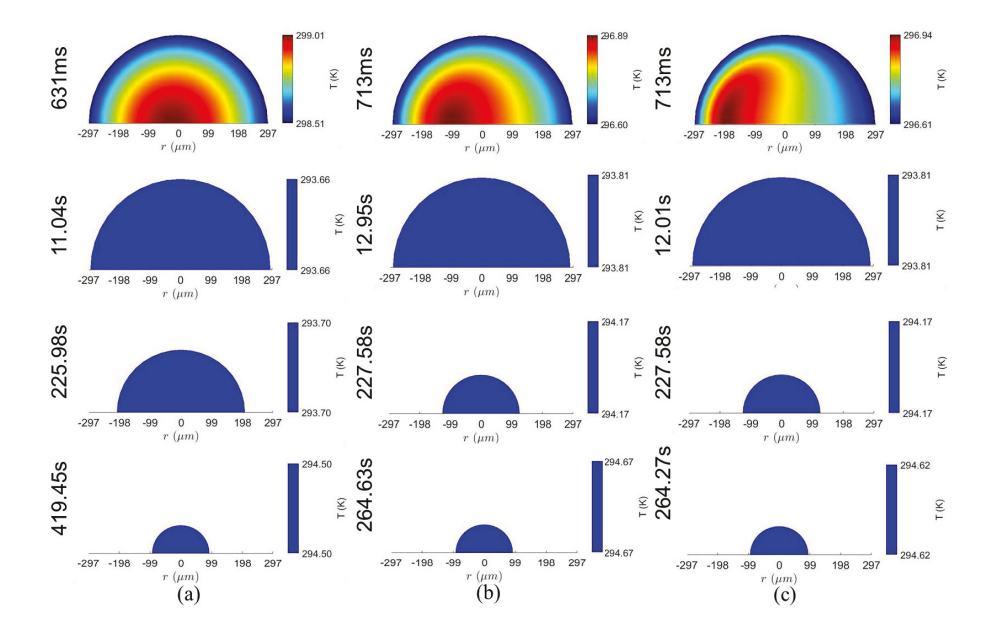


Figure 9: Temperature distribution in liquid phase at different time steps for $D_0 = 594 \mu m$ with initial droplet temperature, $T_0 = 303 K$. The ambient condition is $T_{amb} = 301 K$ and $RH_{amb} = 48\%$. The gas phase perturbation (a) amplitude, a = 0.1 m/s, and frequency, f = 5Hz. (b) a = 1 m/s and f = 5Hz. (c) a = 1 m/s and f = 30Hz.

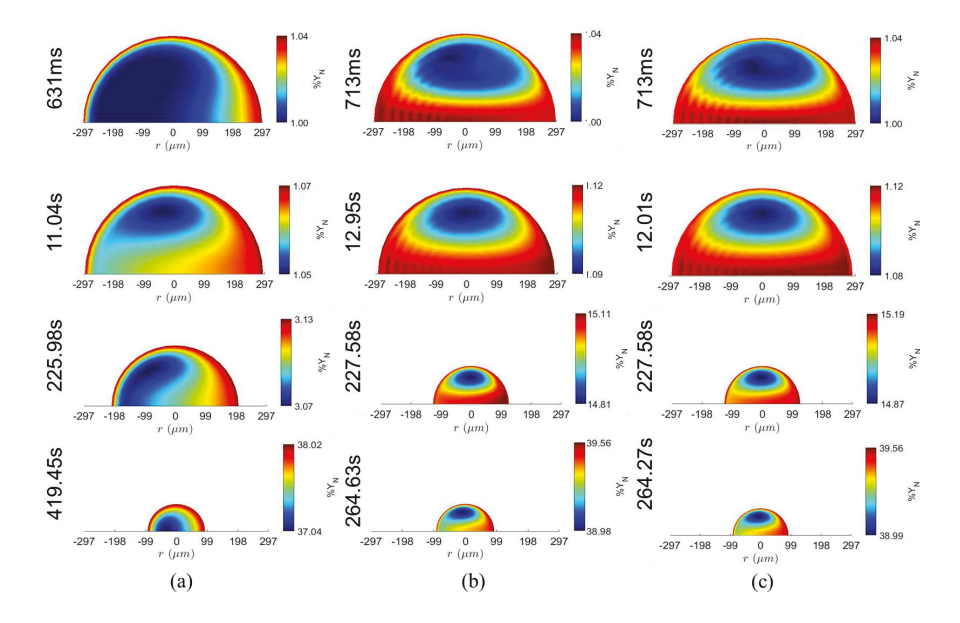


Figure 10: Solute concentration distribution in liquid phase at different time steps for $D_0 = 594 \mu m$ with initial droplet temperature, $T_0 = 303K$. The ambient condition is $T_{amb} = 301K$ and $RH_{amb} = 48\%$. The gas phase perturbation (a) amplitude, a = 0.1 m/s, and frequency, f = 5Hz. (b) a = 1m/s and f = 5Hz. (c) a = 1m/s and f = 30Hz.

- 538 solute concentration, on the other hand, shows stronger advective transport for a larger
- amplitude of oscillation, confirmed by enhanced liquid phase Péclet number. 539
- Acknowledgements. The authors thank Ph.D. students Shubham Sharma and Siddhant Jain for the 540
- experimental data. 541
- Funding. The study at UCSD was partially supported by the U.S. National Science Foundation (CAREER 542
- Award No: CBET-2145210). S.B. gratefully acknowledges the funding received from the DRDO Chair
- 544 Professorship Award.
- 545 **Declaration of interests.** The authors report no conflict of interest.
- Data availability statement. The data can be made available upon reasonable request. 546
- Author contributions. Conceptualization: A.S. and S.B. Methodology: A.S., S.B. and S.M.; Investigation: 547
- S.M. and A.S.; Visualization: S.M. and A.S.; Funding acquisition: A.S. and S.B.; Supervision: A.S. and 548
- 549 S.B.; Writing: original draft: S.M. and A.S.; Writing: editing and revision: S.M., A.S. and S.B.

Appendix A. Effect of evaporation on the scaling analyses 550

- 551 In section 3.4, we used the approximation of constant droplet radius for the scaling analyses.
- Now, we will perform the analyses without assuming a constant droplet radius. It is to be 552
- recognized that a variation in droplet size essentially results in a variation in St with time in 553
- Eq. 3.1. To find a theoretical expression for changes in droplet radius or Stokes number, we can 554
- assume that the droplet quickly attains a steady state (constant temperature and concentration). 555
- Thus, D^2 law (Law 1982), $dr_s^2(t)/dt = -K_v$, can be applied to evaluate instantaneous droplet 556
- radius. Here, the constant K_v can be expressed using B_M , $K_v = 2(\rho_g/\rho_l)\alpha_g \ln(1+B_M)$. It 557
- is to be noted that a similar expression for K_{ν} can also be derived using B_T (Law 1982). 558
- B_M (or B_T) can be evaluated based on the final (steady state) droplet temperature. Here, 559
- α_g is the gas phase thermal diffusivity. It can be seen that K_v dictates droplet lifetime 560
- or evaporation rate. For the ambient conditions used for this study, K_{ν} has a value of 561
- approximately $2.2 \times 10^{-10} m^2/s$. However, for hot-dry and cold-humid ambient conditions, K_{ν}
- 562
- is expected to be larger and smaller, respectively. By substituting Stokes number $(St = \tau/t_g)$ 563
- in d^2 law, we find a regression equation for Stokes number 564

$$\frac{dSt}{d(t/t_g)} = -K_{\nu}(\rho_l/\mu_g). \tag{A 1}$$

- To obtain a time history of droplet velocity, one has to solve the coupled ODEs represented 566
- by Eqs. 3.1 and A 1. Unfortunately, a compact closed-form solution does not exist for this 567
- set of ODEs. We, however, can solve these equations numerically. Based on the analysis 568
- with the evaporating droplet, we present the contour plot of the normalized droplet velocity, 569
- $(U_p U_{p,0})/a$ for a large range of St (Y-axis) and non-dimensional time, t/t_g (X-axis) in 570
- 571
- Visual comparison of Figs. 5a and 11 suggest that the results are practically identical, 572
- although the former used constant radius approximation and the latter did not. We also 573
- plotted the error, defined as the absolute differences between the constant radius and variable 574
- radius methods, in Fig. 12. The difference is less than 1%, confirming that the constant 575
- droplet size assumption is okay. 576

REFERENCES

- ABRAMZON, B & SIRIGNANO, WA 1989 Droplet vaporization model for spray combustion calculations. 577 578 International Journal of Heat and Mass Transfer 32 (9), 1605–1618.
- AGGARWAL, SK, PARK, TWM & KATTA, VR 1996 Unsteady spray behavior in a heated jet shear layer: 579 Droplet-vortex interactions. Combustion Science and Technology 113 (1), 429–449. 580

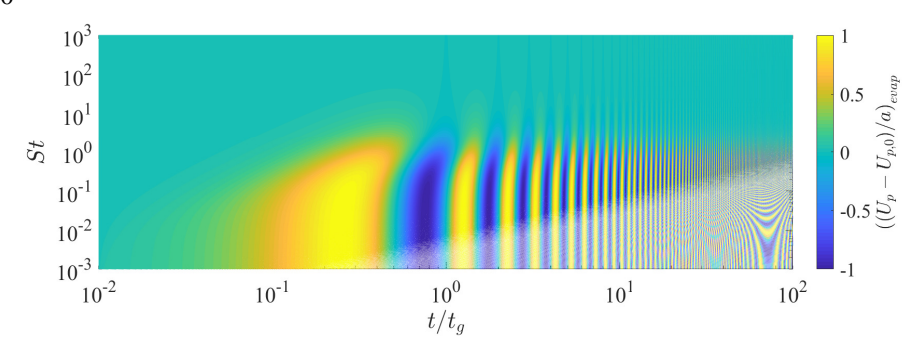


Figure 11: Contour plot of non-dimensional droplet velocity $(U_p - U_{p,0})/a$ with Stokes number (St) and non-dimensional time (t/t_g) , where t_g is the gas phase perturbation time. Here, we used the D^2 law to assess the change in evaporating droplet radius.

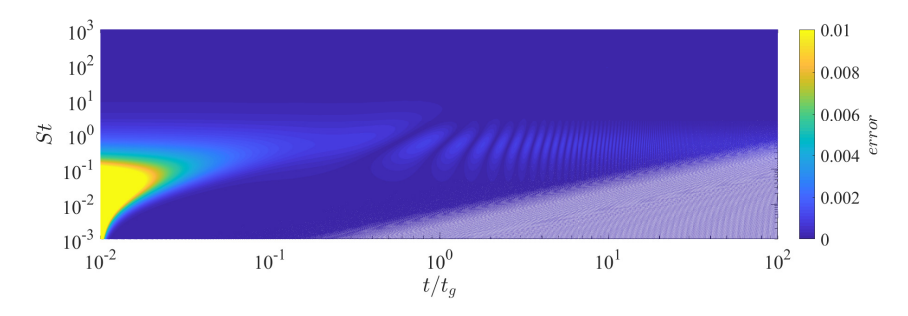


Figure 12: Contour plot of error, defined as the absolute difference in $(U_p - U_{p,0})/a$ using the constant diameter and variable diameter.

AGGARWAL, SK & PENG, F 1995 A Review of Droplet Dynamics and Vaporization Modeling for Engineering Calculations. *Journal of Engineering for Gas Turbines and Power* **117** (3), 453–461.

BADER, A, KELLER, P & HASSE, C 2013 The influence of non-ideal vapor-liquid equilibrium on the evaporation of ethanol/iso-octane droplets. *International Journal of Heat and Mass Transfer* **64**, 547–558.

BALACHANDAR, S, ZALESKI, S, SOLDATI, A, AHMADI, G & BOUROUIBA, L 2020 Host-to-host airborne transmission as a multiphase flow problem for science-based social distance guidelines. *International Journal of Multiphase Flow* 132, 103439.

Basu, S & Cetegen, BM 2008 Modeling of liquid ceramic precursor droplets in a high velocity oxy-fuel flame jet. *Acta materialia* **56** (12), 2750–2759.

BASU, S, JORDAN, EH & CETEGEN, BM 2008 Fluid mechanics and heat transfer of liquid precursor droplets injected into high-temperature plasmas. *Journal of Thermal Spray Technology* **17** (1), 60–72.

Basu, S, Kabi, P, Chaudhuri, S & Saha, A 2020 Insights on drying and precipitation dynamics of respiratory droplets from the perspective of COVID-19. *Physics of Fluids* **32** (12), 123317.

Berlemont, Alain, Desjonqueres, Philippe & Gouesbet, Gérard 1990 Particle lagrangian simulation in turbulent flows. *International Journal of Multiphase Flow* 16 (1), 19–34.

Bhagat, RK, Wykes, MSD, Dalziel, SB & Linden, PF 2020 Effects of ventilation on the indoor spread of COVID-19. *Journal of Fluid Mechanics* **903**.

BIROUK, M & GOKALP, I 2006 Current status of droplet evaporation in turbulent flows. *Progress in Energy and Combustion Science* **32** (4), 408–423.

Borodulin, V Yu, Nizovtsev, MI & Sterlyagov, AN 2019 Evaporation of non-ideal binary solution drops. In *Journal of Physics: Conference Series*, , vol. 1382, p. 012106. IOP Publishing.

BOUROUIBA, L 2020 Turbulent gas clouds and respiratory pathogen emissions: potential implications for reducing transmission of COVID-19. *JAMA* 323 (18), 1837–1838.

BOUROUIBA, L 2021 The fluid dynamics of disease transmission. *Annual Review of Fluid Mechanics* **53**, 473–508.

- BURGER, M, SCHMEHL, R, KOCH, RAINER, WITTIG, S & BAUER, H-J 2006 Dns of droplet-vortex interaction with a karman vortex street. *International Journal of Heat and Fluid Flow* 27 (2), 181–191.
- 609 CANTWELL, B, KARABEYOGLU, A & ALTMAN, D 2010 Recent advances in hybrid propulsion. *International Journal of Energetic Materials and Chemical Propulsion* **9** (4).
- CARPAGNANO, GIOVANNA E, FOSCHINO-BARBARO, MARIA P, CROCETTA, CORRADO, LACEDONIA, DONATO,
 SALIANI, VALERIO, ZOPPO, LUIGI DAVIDE & BARNES, PETER J 2017 Validation of the exhaled breath
 temperature measure: reference values in healthy subjects. *Chest* 151 (4), 855–860.
- CHAUDHURI, S, BASU, S, KABI, P, UNNI, VR & SAHA, A 2020*a* Modeling the role of respiratory droplets in COVID-19 type pandemics. *Physics of Fluids* **32** (6), 063309.
- 616 Chaudhuri, S, Basu, S & Saha, A 2020*b* Analyzing the dominant sars-cov-2 transmission routes toward 617 an ab initio disease spread model. *Physics of Fluids* **32** (12), 123306.
- CHEN, LONGFEI, LIU, ZHIXIN, LIN, YUZHEN & ZHANG, CHI 2016 Different spray droplet evaporation models
 for non-ideal multi-component fuels with experimental validation. *International Journal of Heat and Mass Transfer* 94, 292–300.
- CHONG, KL, NG, CS, HORI, N, YANG, R, VERZICCO, R & LOHSE, D 2021 Extended lifetime of respiratory droplets in a turbulent vapor puff and its implications on airborne disease transmission. *Physical Review Letters* 126 (3), 034502.
- CLEMENS, NT & MUNGAL, MG 1995 Large-scale structure and entrainment in the supersonic mixing layer.
 Journal of Fluid Mechanics 284, 171–216.
- 626 CLIFT, R, GRACE, JR & WEBER, ME 2005 Bubbles, drops, and particles. Courier Corporation.
- 627 CROWE, C, SOMMERFELD, M & TSUII, Y 1998 Multiphase flows with droplets and particles. CRC press.
- DBOUK, T & DRIKAKIS, D 2020 On coughing and airborne droplet transmission to humans. *Physics of Fluids* 32 (5), 053310.
- DWYER, HA, AHARON, I, SHAW, BD & NIAMAND, H 1996 Surface tension influences on methanol droplet
 vaproiation in the presence of water. In *Symposium (International) on Combustion*, vol. 26, pp. 1613–1619. Elsevier.
- DWYER, HA, SHAW, BD & NIAZMAND, H 1998 Droplet/flame interactions including surface tension influences. In *Symposium (international) on combustion*, vol. 27, pp. 1951–1957. Elsevier.
- FANG, BIN, CHEN, LONGFEI, LI, GUANGZE & WANG, LEI 2019 Multi-component droplet evaporation model
 incorporating the effects of non-ideality and thermal radiation. *International Journal of Heat and Mass Transfer* 136, 962–971.
- GRABOWSKI, WW & WANG, L-P 2013 Growth of cloud droplets in a turbulent environment. Annual Review
 of Fluid Mechanics 45, 293–324.
- HARSTAD, K & BELLAN, J 1997 Behavior of a polydisperse cluster of interacting drops evaporating in an
 inviscid vortex. *International Journal of Multiphase flow* 23 (5), 899–925.
- Hubbard, GL, Denny, VE & Mills, AF 1975 Droplet evaporation: effects of transients and variable
 properties. *International Journal of Heat and Mass Transfer* 18 (9), 1003–1008.
- JAYAWEERA, M, PERERA, H, GUNAWARDANA, B & MANATUNGE, J 2020 Transmission of COVID-19 virus by
 droplets and aerosols: A critical review on the unresolved dichotomy. *Environmental Research* 188,
 109819.
- JORDAN, EH, JIANG, C & GELL, M 2015 The solution precursor plasma spray (spps) process: a review with energy considerations. *Journal of Thermal Spray Technology* **24** (7), 1153–1165.
- Kim, I, Elghobashi, S & Sirignano, WA 1995 Unsteady flow interactions between an advected cylindrical vortex tube and a spherical particle. *Journal of Fluid Mechanics* **288**, 123–155.
- KIM, I, ELGHOBASHI, S & SIRIGNANO, WA 1997 Unsteady flow interactions between a pair of advected vortex tubes and a rigid sphere. *International Journal of Multiphase flow* 23 (1), 1–23.
- 653 LAMB, H 1993 Hydrodynamics. Cambridge University Press.
- 654 Law, CK 1982 Recent advances in droplet vaporization and combustion. *Progress in Energy and Combustion* 655 Science 8 (3), 171–201.
- LAW, CHUNG K. 1976 Multicomponent droplet combustion with rapid internal mixing. *Combustion and Flame* **26**, 219–233.
- LAZARO, BJ & LASHERAS, JC 1992 Particle dispersion in the developing free shear layer. part 2. forced flow.
 Journal of Fluid Mechanics 235, 179–221.
- LI, M & CHRISTOFIDES, PD 2009 Modeling and control of high-velocity oxygen-fuel (HVOF) thermal spray: a tutorial review. *Journal of thermal spray technology* **18** (5), 753–768.
- MAJEE, S, SAHA, A, CHAUDHURI, S, CHAKRAVORTTY, D & BASU, S 2021 Two-dimensional mathematical framework for evaporation dynamics of respiratory droplets. *Physics of Fluids* **33** (10), 103302.

- MARCU, B & MEIBURG, E 1996 Three-dimensional features of particle dispersion in a nominally plane mixing layer. *Physics of Fluids* **8** (9), 2266–2268.
- MASOUDI, M & SIRIGNANO, WA 2000 Collision of a vortex with a vaporizing droplet. *International Journal* of Multiphase flow 26 (12), 1925–1949.
- MELLOR, AM 1980 Semi-empirical correlations for gas turbine emissions, ignition, and flame stabilization. *Progress in Energy and Combustion Science* 6 (4), 347–358.
- 670 MITTAL, R, NI, R & SEO, J-H 2020 The flow physics of COVID-19. Journal of Fluid Mechanics 894.
- NAYAR, KISHOR GOVIND, PANCHANATHAN, DIVYA, McKINLEY, GH & LIENHARD, JH 2014 Surface tension of seawater. *Journal of Physical and Chemical Reference Data* **43** (4), 043103.
- Ng, CS, Chong, KL, Yang, R, Li, M, Verzicco, R & Lohse, D 2021 Growth of respiratory droplets in cold and humid air. *Physical Review Fluids* **6** (5), 054303.
- NIAZMAND, H, SHAW, BD, DWYER, HA & AHARON, I 1994 Effects of marangoni convection on transient droplet evaporation. *Combustion science and technology* **103** (1-6), 219–233.
- ODAR, FUAT & HAMILTON, WALLIS S 1964 Forces on a sphere accelerating in a viscous fluid. *Journal of fluid mechanics* **18** (2), 302–314.
- OZTURK, A & CETEGEN, BM 2004 Modeling of plasma assisted formation of precipitates in zirconium containing liquid precursor droplets. *Materials Science and Engineering: A* **384** (1-2), 331–351.
- PAWLOWSKI, L 2009 Suspension and solution thermal spray coatings. *Surface and Coatings Technology* **203** (19), 2807–2829.
- Peaceman, DW & Rachford, Jr, HH 1955 The numerical solution of parabolic and elliptic differential equations. *Journal of the Society for Industrial and Applied Mathematics* **3** (1), 28–41.
- Perini, F & Reitz, RD 2016 Improved atomization, collision and sub-grid scale momentum coupling models for transient vaporizing engine sprays. *International Journal of Multiphase Flow* **79**, 107–123.
- Renksizbulut, M & Yuen, MC 1983 Numerical Study of Droplet Evaporation in a High-Temperature Stream. *Journal of Heat Transfer* **105** (2), 389–397.
- Reveillon, J & Vervisch, L 2005 Analysis of weakly turbulent dilute-spray flames and spray combustion regimes. *Journal of Fluid Mechanics* **537**, 317–347.
- ROSTI, MAE, CAVAIOLA, M, OLIVIERI, S, SEMINARA, AG & MAZZINO, A 2021 Turbulence role in the fate of virus-containing droplets in violent expiratory events. *Physical Review Research* **3** (1), 013091.
- Ruehl, CR, Chuang, PY & Nenes, A 2008 How quickly do cloud droplets form on atmospheric particles?

 Atmospheric Chemistry and Physics 8 (4), 1043–1055.
- 695 Saha, A, Deepu, P & Basu, S 2018 Transport phenomena in functional droplets. In *Droplet and Spray* 696 Transport: Paradigms and Applications, pp. 55–81. Springer.
- 697 Saha, A, Kumar, R & Basu, S 2010 Infrared thermography and numerical study of vaporization 698 characteristics of pure and blended bio-fuel droplets. *International Journal of Heat and Mass Transfer* 699 **53** (19-20), 3862–3873.
- 700 Saha, Abhishek, Majee, Sreeparna, Chaudhuri, Swetaprovo & Basu, Saptarshi 2022 Evaporation 701 and precipitation dynamics of a respiratory droplet. In *Drying of Complex Fluid Drops*, pp. 191–214.
- SAHA, A, SEAL, S, CETEGEN, B, JORDAN, E, OZTURK, A & BASU, S 2009a Thermo-physical processes
 in cerium nitrate precursor droplets injected into high temperature plasma. Surface and Coatings
 Technology 203 (15), 2081–2091.
- SAHA, A, SINGH, V, SEAL, S & BASU, S 2009b Vaporization and precipitation characteristics of cerium nitrate precursor droplets heated by monochromatic irradiation. Surface and Coatings Technology 203 (15), 2102 2115.
- 708 SAZHIN, SS 2006 Advanced models of fuel droplet heating and evaporation. *Progress in Energy and Combustion Science* **32** (2), 162–214.
- SAZHIN, SS 2017 Modelling of fuel droplet heating and evaporation: Recent results and unsolved problems.
 Fuel 196, 69–101.
- SENDA, JIRO, HIGAKI, TOMOHIRO, SAGANE, YASUYUKI, FUJIMOTO, HAJIME, TAKAGI, YASUO & ADACHI,
 MASAYUKI 2000 Modeling and measurement on evaporation process of multicomponent fuels. SAE
 transactions pp. 347–358.
- 715 Sharma, S, Jain, S, Saha, A & Basu, S 2022 Evaporation dynamics of a surrogate respiratory droplet in a vortical environment. *Journal of Colloid and Interface Science* **623**, 541–551.
- 717 Sharma, S, Singh, AP & Basu, S 2021 On the dynamics of vortex–droplet co-axial interaction: insights into droplet and vortex dynamics. *Journal of Fluid Mechanics* **918**.
- 719 Shaw, RA 2003 Particle-turbulence interactions in atmospheric clouds. *Annual Review of Fluid Mechanics* **35** (1), 183–227.

- SHAW, RA, READE, WC, COLLINS, LR & VERLINDE, J 1998 Preferential concentration of cloud droplets
 by turbulence: Effects on the early evolution of cumulus cloud droplet spectra. *Journal of the Atmospheric Sciences* 55 (11), 1965–1976.
- 724 SIRIGNANO, WA 1983 Fuel droplet vaporization and spray combustion theory. *Progress in Energy and Combustion Science* **9** (4), 291–322.
- 726 SIRIGNANO, WILLIAM A 2010 Fluid dynamics and transport of droplets and sprays. Cambridge university press.
- Somsen, GA, van Rijn, C, Kooij, S, Bem, RA & Bonn, D 2020 Small droplet aerosols in poorly ventilated spaces and sars-cov-2 transmission. *The Lancet Respiratory Medicine* **8** (7), 658–659.
- TANG, LF, WEN, F, YANG, Y, CROWE, CT, CHUNG, JN & TROUTT, TR 1992 Self-organizing particle dispersion
 mechanism in a plane wake. *Physics of Fluids A: Fluid Dynamics* 4 (10), 2244–2251.
- VAILLANCOURT, PA & YAU, MK 2000 Review of particle-turbulence interactions and consequences for cloud physics. *Bulletin of the American Meteorological Society* **81** (2), 285 298.
- 734 VAN WYLEN, GJ & SONNTAG, RE 1978 Fundamentals of Classical Thermodynamics. Wiley & Sons, New York.
- VEJERANO, EP & MARR, LC 2018 Physico-chemical characteristics of evaporating respiratory fluid droplets.
 Journal of The Royal Society Interface 15 (139), 20170939.
- WORLD HEALTH ORGANIZATION 2020 Modes of transmission of virus causing COVID-19: implications for ipc precaution recommendations: scientific brief, 29 march 2020. *Tech. Rep.*. World Health Organization.